A novel phase field method for modeling the fracture of long bones

Rilin Shen[a,b,*], Haim Waisman[b,*], Zohar Yosibash[c], Gal Dahan[c]

[a]Department of Astronautic Science and Mechanics, Harbin Institute of Technology, Harbin 150001, China

[b]Department of Civil Engineering and Engineering Mechanics, Columbia University, 610 Seeley W. Mudd Building, 500 West 120th Street, Mail Code 4709, New York, NY 10027, United States

[c]School of Mechanical Engineering, The Iby and Aladar Fleischman Faculty of Engineering, Tel Aviv University, 69978 Ramat Aviv, Israel

---

Abstract

A proximal humerus fracture is an injury to the shoulder joint that necessitates medical attention. While it is one of the most common fracture injuries impacting the elder community and those who suffer from traumatic falls or forceful collisions, there are almost no validated computational methods that can accurately model these fractures. This could be due to the complex, inhomogeneous bone microstructure, complex geometries and the limitations of current fracture mechanics methods.

In this paper, we develop and implement a novel phase field method to investigate the proximal humerus fracture. To model the fracture in the inhomogeneous domain, we propose a power law relationship between bone mineral density and critical energy release rate. The method is validated by an in vitro experiment, in which a human humerus is constrained on both ends while subjected to compressive loads on its head in the longitudinal direction that lead to fracture at the anatomical neck. CT-scans are employed to acquire the bone geometry and material parameters, from which detailed finite element meshes with inhomogeneous Young modulus distribution in the bone are generated.

The numerical method, implemented in a high performance computing environment, is used to quantitatively predict the complex 3D brittle fracture of the bone, and is shown to be in good agreement with experimental observations. Furthermore, our findings show that the damage is initiated in the trabecular bone-head and propagates

*Corresponding author

Email addresses: shenrilin@gmail.com (Rilin Shen), waisman@civil.columbia.edu (Haim Waisman)

outward towards the bone cortex. We conclude that the proposed phase field method is a promising approach to model bone fracture.

Keywords: bone fracture, phase field method, crack propagation, inhomogeneous, energy release rate

1. Introduction

Proximal humerus fractures are common injuries affecting the elderly and other patients who suffer from traumatic impacts or forceful collisions. A proximal humerus fracture is an injury to the shoulder joint that necessitates medical attention. Depending on the specific location and severity of fracture, surgical intervention may be required, in which case the current practice is based on the surgeon's experience and intuition but without any support of quantitative models [1, 2]. In this paper our objective is to derive a novel numerical method capable of accurately predicting the fracture of a humerus bone under complex loading conditions. Furthermore, in the long term such numerical tool may actually assist in surgical decisions. For example, decisions regarding implant insertions in case of bone fracture could be supported by computer simulations and become more reliable. For some patients implants can lead to faster tissue regrowth and bone healing, while in others implants can cause undesired fragmentation, pain, and significant bone damage.

Due to the clinical importance and wide spread of bone fractures, a number of validated bone models have been proposed in the literature [3–7], however, most of them do not account for fracture initiation and propagation, which is a critical issue. This is due to the complex bone constitutive laws, complex geometries and the limitation of current fracture mechanics methods. Bones are natural composite materials, with composition and structure that vary as function of age and sex. The bone structure is hierarchical and thus can be considered to have multiple spatial scales. On the macroscale bones have a hard outer shell-type layer composed of cortical bone and an inner soft porous-type layer called trabecular bone. Thus a first order macro-scale approximation suggest that long-bones can be modeled as elastic, isotropic but highly inhomogeneous materials, which makes the fracture modeling of such bones extremely challenging and adds to the already complex 3D geometry.

For clinical and biomedical applications, a macro-scale approach is typically easier to employ and has therefore been preferred in the literature [7–9]. To this end, Quantitative Computed Tomography (QCT)-based FEM analysis has been employed in the last two decades to predict the strength and crack patterns in bones under different

loading conditions [8–16]. QCT images are usually employed for the generation of 3D finite element meshes and assignment of bone material properties. For example, inhomogeneous Young's modulus can be obtained from the bone mineral density (BMD), which can be directly estimated from the QCT image analysis [9, 17]. Although it has been shown that BMD is not the only factor contributing to bone fracture and may not be an accurate predictor of bone strength [18–20], it is yet a simple approach that provides effective prediction to the risk of fracture.

Modeling the fracture initiation and propagation in bones is challenging and therefore has been primarily addressed in the literature [7, 12, 13, 21–23] indirectly, by development of fracture criteria/indicators based on von Mises stress, equivalent strain and maximum principal strain for human proximal femur fracture. For example, Yosibash and co-workers [7, 13, 21] developed high-order finite element methods (p-FEMs) to predict fracture initiation based on maximum principal strain, which agreed well with experimental results. Keyak and Rossi [23] tested the effectiveness of several stress- and strain- based failure theories, which can account for differences in tensile and compressive material strengths for the proximal femur bone, by using CT scan-based FEMs. However, while these criteria and failure theories can predict crack initiation they cannot model fracture propagation and the post-failure response of the bone. Dragomir-Daescu et al. [12] investigated the fracture of femurs using QCT/FEM analysis with a nonlinear constitutive law for the bone tissue. A yield strain was introduced and once the von Mises strain exceeded it, the Young's modulus was decreased to a very small value. The predicted fracture load and patterns agreed well with their experimental results. A slight mesh dependency of stiffness and strength was observed.

Numerical methods used to model crack initiation and propagation can in general be grouped into two main categories: fracture mechanics based approaches and Continuum Damage Mechanics (CDM) methods. Hambli and co-workers [6, 24, 25] modeled the fracture process based on element deletion technique. They developed an FEM model of the proximal femur based on continuum damage mechanics (CDM) to obtain full force-displacement curves under stance condition. A coupled quasi-brittle damage law was implemented and a weighted strain criterion with a characteristic crack length was used to alleviate the mesh sensitivity. This model was also applied to model trabecular bone damage and fracture [26]. Harrison et al. [27] proposed a 3D voxel based FE model to simulate the complete fracture of ovine vertebral trabecular bone samples by incorporating damage growth and fracture criteria. A cohesive parameter representing the damage and crack propagation was simulated by the element deletion technique. Cohesive FEM has also been employed to study fracture of bones at the

macro-scale. With this technique, Ural and Mischinski [28] investigated crack growth, fracture strength and loss of toughness in human distal radius, considering the effects of aging, intra-cortical porosity and strain rate. Inserting cohesive elements along the expected crack area limit its ability to model complex fracture profiles. Abdel-Wahad and Silberschmidt [29] employed the extended finite element method (XFEM) to model the impact strength of cortical bone tissue. The simulation results agreed well with the experimental data. Multiscale methods based on homogenization theory have also been proposed to model bone fracture [30], but those may be computationally too demanding. Nonetheless, these two classes of methods may be limited when applied to bone fracture. For example, the complex bone geometry and inhomogeneous material properties makes the implementation of discrete methods extremely difficult [31], and on the other hand damage methods tends to be either mesh dependent (local damage) [32] or spread the damage over large unrealistic domains (nonlocal damage) [33, 34].

To this end, a so-called phase field method (PFM) for modeling brittle fracture has emerged in the last two decades [35–46], and was shown to overcome some of the aforementioned limitations of the other methods. Similar to nonlocal damage mechanics, the PFM is also a regularized continuum based method that can model crack initiation and propagation in complex three-dimensional geometries. However, as opposed to nonlocal damage methods, this approach is based on energy minimization principles and yields narrow crack bands, which seems more realistic for brittle and quasi-brittle fracture. Two critical parameters are used in this method, namely a length scale parameter l_0, which controls the crack width, and a Griffith-type critical energy release rate G_c, which is a material property that serves as a fracture driving force criteria [47]. It should be noted that the phase field method converges to a discrete crack in the limit when l_0 goes to zero [37].

The PFM was applied to a range of materials, such as polymers [48], asphalt [49], concrete [50] and polycrystalline materials [51], including brittle and quasi-brittle fracture [38, 52], ductile fracture [46, 53], hydraulic fracture [54–56], interfacial fracture [57, 58] and anisotropic fracture [59, 60]. More details and comparisons of the phase field method and traditional damage mechanics could be found in [33, 61]

In this paper we propose an important modification to the phase field method for modeling the fracture of highly inhomogeneous materials, as the proximal humerus fracture studied in this paper. Specifically, we propose a power-law relationship between bone mineral density and critical energy release rate to account for the unique bone structure. The method is validated by an in vitro experiment on a human humerus subject to compressive loads. CT-scans are employed to acquire bone geometry and

material parameters, from which detailed finite element meshes and predications are obtained.

The paper is organized as follows: In section 2, the fundamentals of the phase field method are presented with a brief overview of the fracture mechanics related aspects of the method; In section 3, a Method of Manufactured solutions (MMS) is utilized to verify the implementation and convergence of the method. In section 4, we first briefly describe the experiment that was conducted in [21] and the corresponding finite element model that is considered in this work, including the humerus-bone geometry, boundary conditions applied in the experiment, finite element mesh and material properties. An educated assumption of a power-law relation between the critical energy release rate and the density is introduced. Second, we calibrate a few critical parameters in the model including: the power-law exponent and the length scale size against the strain-force curves recorded in the experiment. Third, we provide the 3D crack propagation simulations obtained with our calibrated parameters and illustrate the location of crack initiation and propagation. We also demonstrate the parallel scalability of the model. Finally, concluding remarks are drawn to summarize our research findings.

2. Fundamentals of the phase field method

2.1. Phase field representation of a crack

The key idea of the phase field method is to represent fracture as a continuum entity with a small finite width rather than a strict discontinuity, in which the stiffness of the material within that width is significantly reduced or damaged. In this formulation, a surface density function, which depends on the fracture width l_0 can be used to represent the crack without the need to explicitly track the discontinuity.

To illustrate the underlying concepts of the phase field method, consider an infinitely long one-dimensional bar pulled on both sides with a discrete crack at $x = 0$. As illustrated in Figure 1, the phase field approximation of a discrete crack can be viewed from a continuum point of view as a smeared crack with the following approximation [52]:

$$c = e^{-\frac{|x|}{2l_0}}. \tag{2.1}$$

Here, c is the phase field variable and x is the longitudinal axis. The phase field variable

$c \in [0,1]$ satisfying:

$$\begin{aligned} c(0) &= 1 \\ c &\to 0 \quad \text{as} \quad x \to \pm\infty \\ c_{,x} &\to 0 \quad \text{as} \quad x \to \pm\infty \end{aligned} \tag{2.2}$$

Note that l_0 is a regularization parameter that controls the smeared crack width, however, it should be emphasized that l_0 doesn't represent the actual width. Crack topologies for four different l_0 values are shown in Figure 1(b). When l_0 decreases to 0, the smeared crack representation converges to a discrete crack.

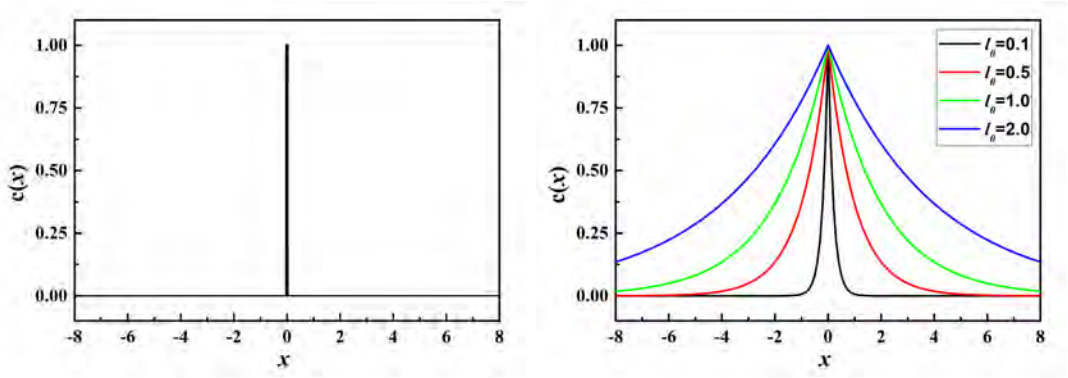

Figure 1: Schematic depiction of a smeared crack representation with the phase field method (a) discrete crack representation, and (b) phase field representation of the discrete crack. Crack topologies with different l_0 values are illustrated in the right figure.

The first and second derivatives of the phase field function with respect to x are given by

$$\begin{aligned} c_{,x} &= -\frac{sgn(x)}{2l_0} e^{-\frac{|x|}{2l_0}} \\ c_{,xx} &= -\frac{1}{4l_0^2} e^{-\frac{|x|}{2l_0}} = -\frac{1}{4l_0^2} c \end{aligned} \tag{2.3}$$

where *sgn* denotes the sign of x.

With the above definitions, for $x \neq 0$, Eq.2.1 is the solution to the homogeneous differential equation

$$c - 4l_0^2 c_{,xx} = 0 \text{ in } \Omega \tag{2.4}$$

where Ω denotes the domain of bar.

The corresponding quadratic functional is

$$I(c) = \int_{-\infty}^{\infty} \frac{1}{2}\left[c_{,x}^2 + \frac{1}{4l_0^2}c^2\right] dx \tag{2.5}$$

where the differential equation 2.4 is the solution of the Euler-Lagrange equation resulting by minimization of

$$c^\star = \underset{c\in\mathbb{S}}{\operatorname{argmin}}\{I(c)\} \tag{2.6}$$

where $\mathbb{S} = \{c \in H^1 | c(0) = 1, c(\pm\infty) \to 0, c_{,x}(\pm\infty) \to 0\}$ and H^1 is the Sobolev space.

Substituting Eq.2.1 into Eq.2.5 yields

$$I(c^\star) = \frac{1}{2l_0} \tag{2.7}$$

For convenience, one may rewrite the functional with a scaling factor as follows

$$\begin{aligned} \Gamma_s = 2l_0 I(c) &= \int_\Omega \left[\frac{1}{2}\left(\frac{1}{2l_0}c^2 + 2l_0 c_{,x}^2)\right)\right] d\Omega \\ &= \int_A \int_{-\infty}^{\infty} \left[\frac{1}{2}\left(\frac{1}{2l_0}c^2 + 2l_0 c_{,x}^2)\right)\right] dx dA = A \end{aligned} \tag{2.8}$$

where A is the cross-sectional area of the bar. Clearly, the minimization of this equation gives the crack topology given in Eq.2.1, where Γ_s can be interpreted as a crack surface density where the integrand of Eq.2.8 is

$$\gamma(c, c_{,x}) = \frac{1}{4l_0}c^2 + l_0 c_{,x}^2 \tag{2.9}$$

When the above theory is extended to multi-dimensions, the crack surface density can expressed as

$$\gamma = \frac{1}{4l_0}c^2 + l_0 c_{,i} c_{,i} \tag{2.10}$$

where Einstein's summation convention is assumed and $i = 1, ...d$ with d being the number of dimensions.

2.2. Governing equations

For elastic solids, the total free energy Π is additively decomposed into two parts:

$$\Pi = \Pi_e + \Pi_f = \int_{\Omega} \psi_e dV + \int_{\Gamma_d} \psi_f dA \tag{2.11}$$

where Π_e and Π_f are the elastic energy stored in the solid and the fracture energy needed to create new crack surfaces, respectively. Here, ψ_e and ψ_f denote the corresponding energy density functions.

To account for different fracture modes, the elastic strain energy density is split into two parts:

$$\psi_e = W^- + m(c)W^+ \tag{2.12}$$

where W^- and W^+ represent the damaged and undamaged strain energy densities, respectively. $m(c)$ is the degradation function used to degrade the stiffness within the smeared crack representation. The degradation function implies a reduction of the stiffness in the regions of the domain that have no compressive stresses, i.e. $C^d_{ijkl} = m(c)C_{ijkl}$, where C^d_{ijkl} and C_{ijkl} are the damaged and undamaged material stiffness matrix, respectively. The precise model that degrades the stiffness depends on the type of energy splitting in Eq.2.12.

In general, two kinds of strain energy split methods have been proposed in the literature, volumetric-deviatoric split and a spectral decomposition split [35, 46]. In the current work we adopt the volumetric-deviatoric split, which can be expressed as:

$$W = \frac{1}{2} C_{ijkl}\varepsilon_{ij}\varepsilon_{kl} \tag{2.13}$$

$$W^- = K\langle \varepsilon_{ii} \rangle_-^2 \tag{2.14}$$

$$W^+ = K\langle \varepsilon_{ii} \rangle_+^2 + \mu \varepsilon_{ij}^{dev} \varepsilon_{ij}^{dev} \tag{2.15}$$

where ε_{ij} is strain tensor and $\varepsilon_{ij}^{dev} = \varepsilon_{ij} - \frac{1}{3}\varepsilon_{kk}\delta_{ij}$ is the deviatoric strain tensor. The volumetric modulus K and shear modulus μ are related to Young's modulus E and Possion's ratio ν as follows: $K = \frac{E}{3(1-2\nu)}, G = \frac{E}{2(1+\nu)}$. $\langle \cdot \rangle$ is Macaulay brackets defined as:

$$\langle x \rangle_+ = \begin{cases} x & if\ x \geq 0 \\ 0 & if\ x < 0 \end{cases} \qquad \langle x \rangle_- = \begin{cases} x & if\ x \leq 0 \\ 0 & if\ x > 0 \end{cases} \tag{2.16}$$

With the above definition, the stress can be expressed as

$$\sigma_{ij} = \sigma_{ij}^{-} + m_c \sigma_{ij}^{+} = \frac{\partial W^{-}}{\partial \varepsilon_{ij}} + m_c \frac{\partial W^{+}}{\partial \varepsilon_{ij}} \tag{2.17}$$

Hence, the volumetric-deviatoric split of the energy implies that the stiffness will be degraded as a result of non compressive hydrostatic stress components as well as deviatoric stress components. Such splitting might better capture a shear dominated fracture [35].

In this paper, we consider a generic cubic depredation function of the form $m(c) = [1+(2-s)c](1-c)^2$ [62], which by varying s could provide a response ranging from brittle to ductile type failures. That is, when $s \to 0$ the response is nearly linear elastic prior to fracture with an abrupt fracture response. However, when $s = 2$ the degradation function reduces to a quadratic form and the response resembles a ductile type failure [52]. It should also be noted that the ductile type failure has better convergence characteristics, i.e. it requires less nonlinear iterations to converge, since the failure response is more gradual and less abrupt than brittle fracture. In the current work we choose $s = 0.8$ which is yields a quasi-brittle response with good convergence behaviour.

The fracture energy is related to surface energy given in Eq.2.9, which can be approximated by

$$\Pi_f = G_c \int_{\Omega} \gamma(c, c_{,i}) dV \tag{2.18}$$

where G_c is a Griffith-type critical energy release rate of the material (given material parameter). Substituting Eq. 2.10, Eq. 2.12, and Eq. 2.18 to Eq. 2.11, the free energy reads

$$\Pi = \int_{\Omega} \left[W^{-} + (m(c) + \eta) W^{+} \right] dV + G_c \int_{\Omega} \gamma(c, c_{,i}) dV \tag{2.19}$$

where the scalar η is introduced and taken to be a small value, $\eta = 0.0001$ to avoid numerical ill conditioning in the case of complete failure of an element in the mesh.

For a given equilibrium state, the free energy Π must be a minimum, which requires the variation of the Eq. 2.19 to be zero:

$$\delta\Pi = \frac{\partial \Pi}{\partial \varepsilon_{ij}} \delta\varepsilon_{ij} + \frac{\partial \Pi}{\partial c} \delta c + \frac{\partial \Pi}{\partial c_{,i}} \delta c_{,i} \tag{2.20}$$

Eq. 2.20 should hold for any arbitrary admissible $\delta\varepsilon_{ij}, \delta c$ and $\delta c_{,i}$, which leads to the

coupled governing equations [63],

$$\text{Equilibrium:} \qquad \sigma_{ij,j} = 0 \tag{2.21}$$

$$\text{Phase-Field evolution:} \qquad c = 4l_0^2 c_{,ii} - \frac{2l_0}{G_c}\frac{\partial m}{\partial c}\mathscr{H} \tag{2.22}$$

where the first equation is the divergence of stress σ_{ij} in the absence of body forces, and the second equation is the crack driving law which resembles the ODE given in Eq. 2.4. The history variable scalar $\mathscr{H} = max(W^+)$ is introduced to enforce irreversibility of damage, which means that damage can only grow, i.e. $\dot{c} \geq 0$ [52].

The boundary conditions associated with this problem are given as

$$\begin{cases} c_{,i} & = 0, \text{ on } \Gamma^c \\ n_j \sigma_{ij} & = \bar{T}_i, \text{ on } \Gamma^T \\ u_i & = \bar{u}_i, \text{ on } \Gamma^u \end{cases} \tag{2.23}$$

where the first equation means that damage flux cannot flow out of the system, the second corresponds to Neumann boundary conditions on tractions, where n_j is the normal to the surface, and the third are Dirichlet conditions on the displacements u_i.

Finally, we note that two key parameters should be considered carefully when employing and implementing the phase field method: the length scale l_0 and the critical energy release rate G_c.

Remark 1: While the smaller the length scale l_0 is, the closer the fracture representation is to true cracks. However, computational limitation preclude extremely small length scales [42, 64–66]. It is recommended that one should have at least two elements across the smeared crack width, which means the element size must be at least twice smaller than the length scale [64]. Nonetheless, to avoid some of those computational limitations, l_0 can be related to the Young's modulus, critical energy and the strength of the material and could be directly be calibrated against experimental results, as suggested in [62, 64].

Remark 2: The critical energy release rate G_c is usually assumed to be the critical energy release rate under tension. However, for many materials the energy release rate under tension might be quite different from the one under shear. Hence, although in the current work we follow the assumption that G_c corresponds to tension, one should consider G_c in relation to the dominant energy release rate or incorporate both tension

or shear, as proposed in [65]

Remark 3: Note that for inhomogeneous materials the critical fracture G_c should also be varying in the domain. Several research groups in the biomechanics community have argued for a strong correlation between the density and the energy release rate [1, 67–70]. In the current paper, we propose a power-law dependency between the critical energy release rate G_c and the bone mineral density at a given material point. More details are discussed in Section 4.3.

3. Model Verification: Method of manufactured solutions

We employ the Method of Manufactured Solutions (MMS) to verify the implementation of the phase field method [71, 72]. MMS is a well known procedure used for verification of nonlinear coupled codes and has been widely used in engineering analysis.

In the phase field method, one needs to manufacture displacements and phase field solutions, which are then substituted into the governing equations to generate additional source terms as well as initial/boundary conditions. These predefined fields are then compared with the predicted output of the code in terms of displacement, phase field, and stress fields and the convergence rates can be examined.

Consider a 2D squared computational domain $\{0.0 \leq x \leq 0.1, 0.0 \leq y \leq 0.1\}$. The convergence tolerance is set to 1.0E-16. Six different meshes, 8×8, 20×20, 32×32, 40×40, 50×50 and 64×64 are utilized to examine the convergence. The solution of the FEM with bilinear type quad elements is compared with the manufactured fields. Poisson's ratio of $\nu = 0.3$ and a length scale of $l_0 = 0.02$ are assumed.

Unstructured meshes are used to avoid mesh alignment effects and the average mesh size is estimated as,

$$h_{ave} = \sqrt{\frac{A_{total}}{N_{ele}}} \tag{3.1}$$

where A_{total} is the area of problem domain and N_{ele} is the number of elements.

The L_2 norm is used to evaluate the relative error between the exact and numerical solutions, which is given as

$$err = \frac{||\boldsymbol{u}_{exa} - \boldsymbol{u}_{num}||_2}{||\boldsymbol{u}_{exa}||_2} \tag{3.2}$$

where $\boldsymbol{u}_{exa}$ and $\boldsymbol{u}_{num}$ are manufactured solutions and numerical results, respectively.

We have studied both homogeneous and inhomogeneous materials. However, in this section we will only report the verification of the code when applied to inhomogeneous materials, in which Young's modulus variability is defined by

$$E = E_0 \left(1 - \frac{E_2}{e^{E_1\sqrt{(x-x_0)^2+(y-y_0)^2}} + e^{-E_1\sqrt{(x-x_0)^2+(y-y_0)^2}}} \right) \tag{3.3}$$

and the manufactured solutions for displacement and phase field are assumed to be

$$\begin{aligned} u_x &= a_1 x + a_2 y + a_0 \\ u_y &= b_1 x + b_2 y + b_0 \\ c &= \frac{c_0}{e^{c_1\sqrt{(x-x_0)^2+(y-y_0)^2}} + e^{-c_1\sqrt{(x-x_0)^2+(y-y_0)^2}}} \end{aligned} \tag{3.4}$$

where the constants $E_0, E_1, E_2, a_0, a_1, a_2, b_0, b_1, b_2, c_0, c_1, x_0, y_0$ are selected as 200.0E9, 100.0, 0.1, 0.0, 0.002, 0.0015, 0.0, 0.001, -0.006, 1.6, 100, 0.05, 0.05, respectively. These functions and parameters generate a hole-like imperfection in the center of the domain and the model experiences shear, tension deformation along x direction and compression along y direction. Note that for these constants, the term in the parenthesis of Eq. 3.3 ranges between [0.95,1).

Substituting Eq.3.3 and 3.4 into the governing equations, we obtain three source terms and corresponding boundary conditions, which are then implemented in the code. The numerical results and the manufactured results for the fine mesh are shown as Fig. 2. It can be seen that the numerical results agree well with the manufactured solutions. Also, the error in the displacements field and phase field with respect to the mesh size h_{ave} are plotted in log-log scale as shown in Fig.3, in which the convergence rates are also presented. Convergence rates are obtained by least-square fitting. All the studied fields show good convergence which indicates that our implementation is verified.

4. Model configuration: experiments and simulations

4.1. Mechanical experiments on a human humerus

The mechanical experiments performed in [73] are considered in this paper. Fig.4 shows the experimental setup of the humerus bone and the position of strain gauges used to measure the strains in the experiments. This humerus is taken from a 67 years-old male donor, 1.78 m (70") tall and weight of 84 kg (186 lb), who died from an end stage heart failure. The bone was obtained from the National Disease Research Interchange

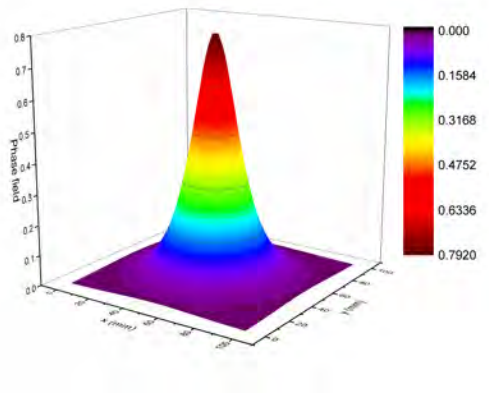

(a) Analytical phase field

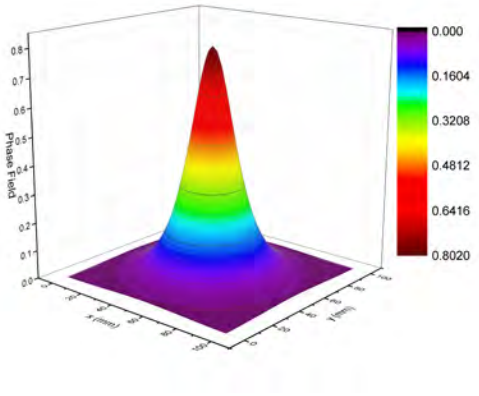

(b) Numerical phase field

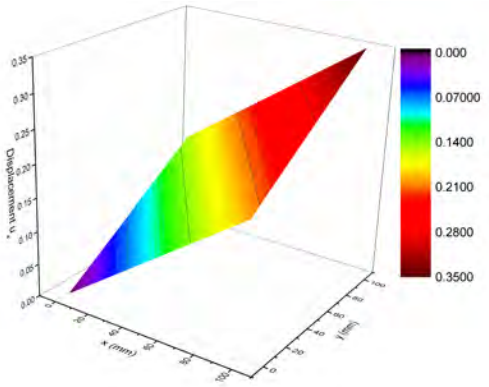

(c) Analytical displacement u_x

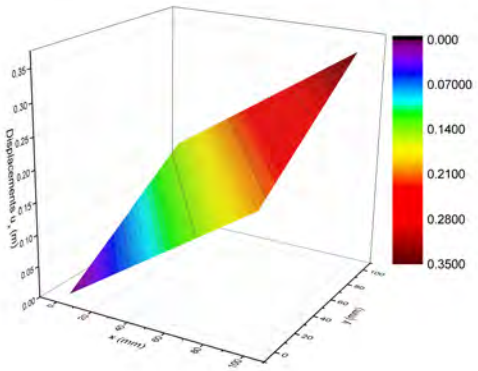

(d) Numerical displacement u_x

Figure 2: Comparison of analytical manufactured solutions and numerical results plotted on the finest 64×64 mesh.

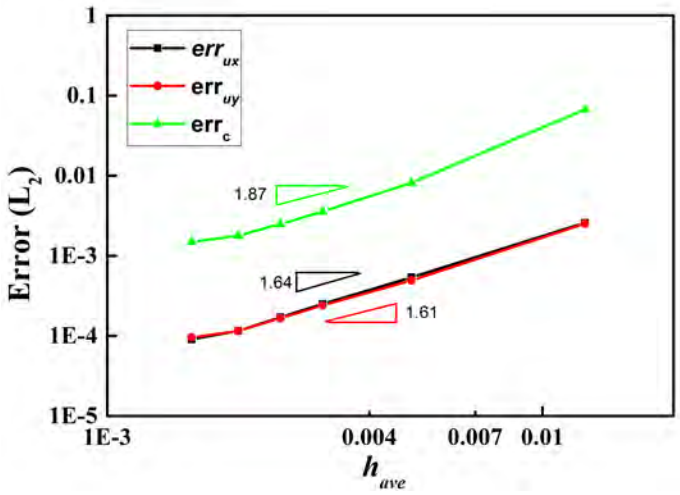

Figure 3: Convergence studies for displacements u_x, u_y and phase field c. Rates of convergence are given in the plot.

(NDRI). The total length along the bone shaft axis is 168mm. The humerus was rotated at 25° about its longitudinal axis to align in the scapular plane, and then fixed to the load cell at a 20° angle. While facing downwards, its head was fixated using a screw to a PMMA base with diameter of 20mm (all angles are relative to a coordinate system on the humerus defined by Wu et al. [74]). This fixation assures a contact area which is constant both in size and location; and prevents the head from moving in the lateral direction which will cause fracture at the distal end rather then at the neck, as illustrated in Fig.4. A displacement of $\approx$ 8mm was applied to the humeri until fracture was observed. Resulted loads on the bone (all 3 components) were measured using a 6-axis load cell (ATI Omega 191). The magnitude of the resultant load applied on the head was 5200N. The z-axis in global coordinate system was set to be along the bone shaft axis and the $x-y$ plane was located on the cross-section of the distal end.

Fourteen uniaxial strain gauges were attached to bone surface and recorded the strain history in the experiment, as shown in Fig.4(b). However, only two of them, #8 and #12, are currently used in our numerical results for calibration and analysis of the model. These two sensors are closer to the fracture region and provide sufficient information necessary to validate the key failure mechanisms of the bone. The coordinate system is shown in Fig.4(b) and the corresponding positions as well directions of these two strain gauges are described in more details in Appendix A.

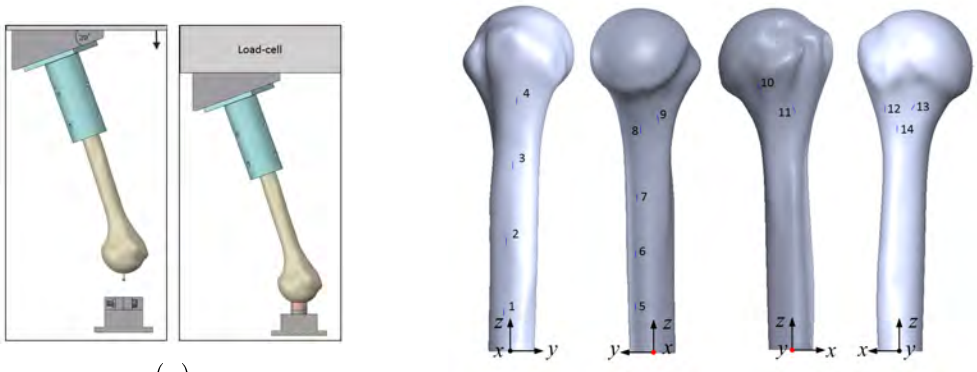

(a) (b)

Figure 4: Compression test of the humerus-bone; (a) The experiment setup; (b) Strain-gauges' positions used to measure strains. Red and black dots denotes the axis in-plane and out of plane directions, respectively. Among them, strain gauge #8 is along the bone shaft axis and #12 is closer to the fracture area.

The reaction force along the z-direction as applied to the bone head was recorded in the experiment, and are used herein to validate the numerical results.

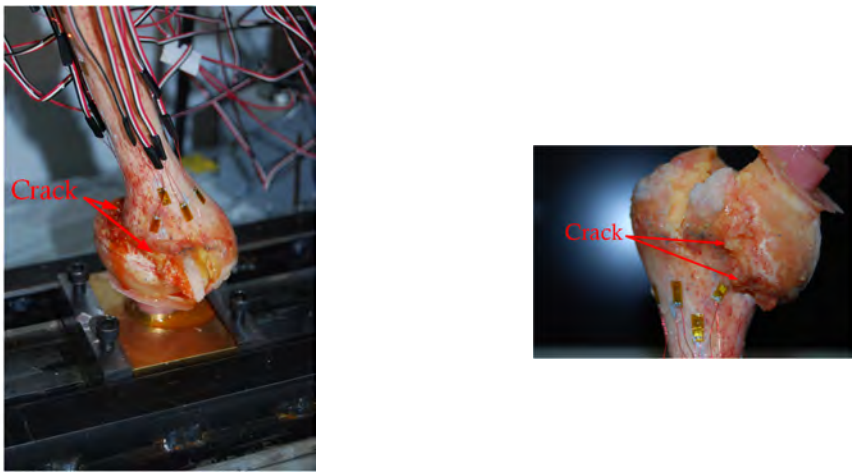

(a) Fracture location (b) Enlarged view of the fracture location

Figure 5: Experiment conducted on a human humerus (67 year old male donor) showing the location of fracture.

4.2. Numerical setup

Parallel Finite element implementation of the phase field method for fracture modeling of the humerus-bone is developed and the simulations are carried out on parallel computers at Columbia University. Details on the implementation of the code is provided in Section 4.4.

The geometric model and the corresponding boundary conditions are illustrated in Fig.6(a). The distal end is clamped while a surface traction pressure, as recorded in the experiments, is applied on top of the bone at the red circle area shown in the figure. The purple lines in the figure denote the locations of strain gauges #8 and #12 similar to the experiments. In Fig.6(b), the bone head is magnified to show the details of the applied tractions. Since the normal directions on every point of the loading area are almost the same, the normal direction $\boldsymbol{n} = \{-0.3119, 0.1085, 0.9439\}$ at the center of the loading area is used in the analysis. A local load system denoted by (x_l, y_l, z_l) is created, in which the surface traction loading is applied. z_l coincides with the normal direction of the surface. Hence, the three components of the resultant traction $\bar{\boldsymbol{T}}$ along local directions are -0.0588,0.517764 and -2.4756 MPa, respectively. Blue point A, as shown in Figure. 6 (b), is the center of the loading area, of which the displacement u_z is extracted to show the loading process in the result section.

In order to obtain an accurate crack path, a very fine mesh that consists of 323,543 linear tetrahedral elements and 58,885 nodes with 4 dofs (three displacements components and one phase field c) per node is generated as shown in Fig.6(c).

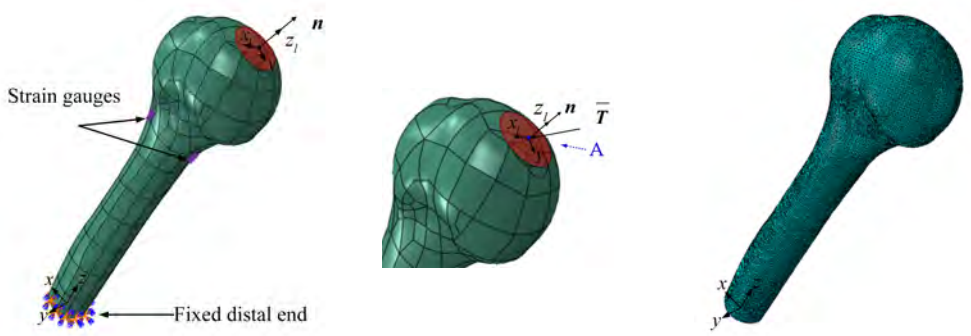

(a) (b) (c)

Figure 6: The humerus-bone model configuration. (a) Bone geometry and boundary conditions. The distal end is fixed and a surface traction is applied on the proximal head (highlighted by the red color); (b) Magnification of the head area in the region of applied surface tractions denoted in red. $\bar{\boldsymbol{T}}$ is the resultant surface traction. Blue point A denotes where the displacement u_z is extracted to show the loading process; (c) The bone model with very fine mesh.

4.3. Material properties

On the macroscale, bones have a hard outer shell-type layer composed of cortical bone and an inner soft porous-type layer, so-called trabecular bone. Thus a first order macro-scale approximation suggest that bones can be modeled as elastic, isotropic but strongly inhomogeneous materials. Nonetheless, adding the aforementioned material properties to the already complex 3D geometry, makes the fracture modeling extremely challenging.

As indicated in references [18, 68–70, 75], the mechanical properties of bone can be expressed in terms of the Bone Mineral Density (BMD) quantity. Various density measurements such as ash density ρ_{ash}, wet density ρ_{wet} and dry density ρ_{dry} have been used in the literature for different modeling purposes. More details regarding density measurements can be found in [76]. The relations between ash density(ρ_{ash}) of the bone and its Young's modulus $\boldsymbol{E}$, documented in Keyak et al. [77] and Keller [3], were shown to provide agreeable results compared with in-vitro experiments. In the current work, we assume similar relations given as

$$E_{cor} = 10200\rho_{ash}^{2.01}(MPa), \qquad \rho_{ash} \geq 0.486(g/cm^3) \tag{4.1}$$

$$E_{mix} = 2398(MPa), \qquad 0.3 < \rho_{ash} < 0.486(g/cm^3) \tag{4.2}$$

$$E_{tra} = 33900\rho_{ash}^{2.2}(MPa), \qquad \rho_{ash} \leq 0.3(g/cm^3) \tag{4.3}$$

where the subscript *cor* and *tra* represent cortical and trabecular regions of the bone, respectively. Subscript *mix* denotes the region that could not be distinguished as cortical or trabecular bone. Figure 7 shows the density distribution of the bone. It can be

seen that there is a thin layer surrounding the bone head area, so-called cortical shell. However, in some regions this shell is extremely thin and practically does not appear in Figure 7c, which indicates weak regions that may lead to fracture initiation.

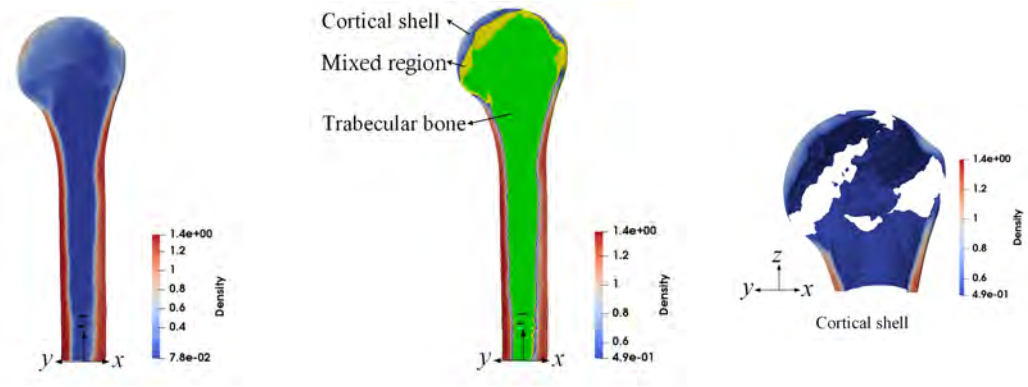

(a) (b) (c)

Figure 7: Density distribution of the humerus. (a) Cross-section of the bone; (b) Different regions defined in Eq.4.1. Mixed region (Yellow area): $0.3 < \rho_{ash} < 0.486$, trabecular bone (Green area): $\rho_{ash} < 0.3$ and Cortical shell (Outer thin layer): $\rho_{ash} > 0.486$. The legend is only for outer thin layer. (c) Closeup view of the cortical shell (all the other regions are not shown in the plot). The units in the legend are given in g/cm^3.

Due to the complexity of bones, many experiments have been conducted to acquire relations between the mechanical behavior of the bone and its properties. Many authors [2, 18, 67–69, 78] have investigated the fracture toughness of bones with different testing methods. Those have led to relations between fracture toughness and age, density and compositions, which are commonly used to evaluate the bone properties.

In addition, experimental results obtained by different groups [1, 67–70] have established empirical relations between density and critical energy release rate. While there is a wide scatter in these empirical models, perhaps due to the diverse testing methods, machine settings and bone age samples, they all suggest that a strong correlation between the density and the energy release rate exist. Hence, one of the goals of this paper is to examine and calibrate the most appropriate relation through numerical parametric studies.

To this end, we propose a power-law dependency between the critical energy release rate G_c and the Young's modulus E (that is related to the bone density ρ_{ash}) at a given material point, written as

$$G_c = G_c^0 \left(\frac{E}{E_0} \right)^{\beta} \tag{4.4}$$

where G_c^0 and E_0 serve as the reference critical energy and Young's modulus, respectively. β is the power-law exponent that describes the relations between Young's modu-

lus and critical energy release rate. $\beta = 0$ means a constant critical energy in the bone, whereas $\beta = 1$ represents a linear relation, and $\beta > 1$ describes a stronger correlation between the energy release rate and Young's modulus at a given material point.

The assignment of material properties such as density, Young's modulus and critical energy release rate is described herein. A file containing the node label and coordinates are exported from Abaqus [79], which is employed here for mesh generation, and then imported to a Python script to assign each node its density from the closet point found in the CT data. A nodal-wise density field is defined, i.e. four different densities per each linear tetrahedral element. The Young's modulus $E(x_i, y_i, z_i)$ and the associated critical energy $G_c(x_i, y_i, z_i)$ at each node are then computed based on Eq.4.1 and 4.4. The corresponding material properties at Gauss points can also be obtained by using the FE shape functions to interpolate the values and compute element stiffness matrices.

The variation of the Young's modulus field throughout the bone model is shown in Fig.8(a). Red and blue colors denotes high and low Young modulus regions, respectively. Fig.8(b) shows a longitudinal slice of the bone, where the green dashed line denotes the boundary between cortical and trabecular bone. It can be seen that the bone head/neck has the lowest Young modulus, which is to say, the most fragile area. Furthermore, a thin stiff shell at the outer region of the cortical bone can also be identified, as illustrated in Fig.8(b).

Fig.9 illustrates the variation of critical energy release rate within the bone. Various β values yield slightly different critical energy distributions. Based on the power-law defined in Eq.4.4, the distribution is comparable with the experiment in [80]. As observed in the figure, the head and neck of the bone is the most fragile region of the bone and is where most fractures occur under external loading. The Poisson's ratio is assumed to be 0.3 throughout the model.

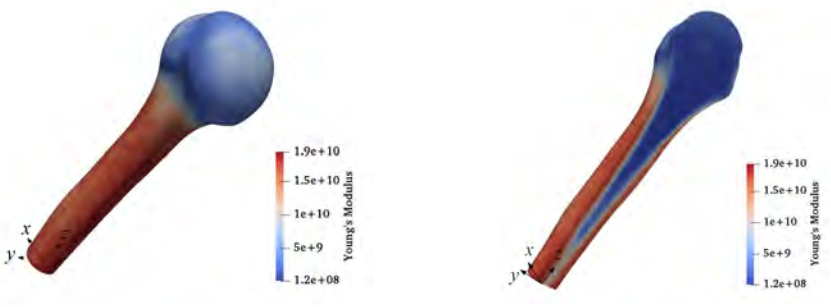

(a) (b)

Figure 8: Variation of Young's modulus in the bone. (a) Entire bone ; (b) Cross-section of the bone. The units in the legend are given in Pa.

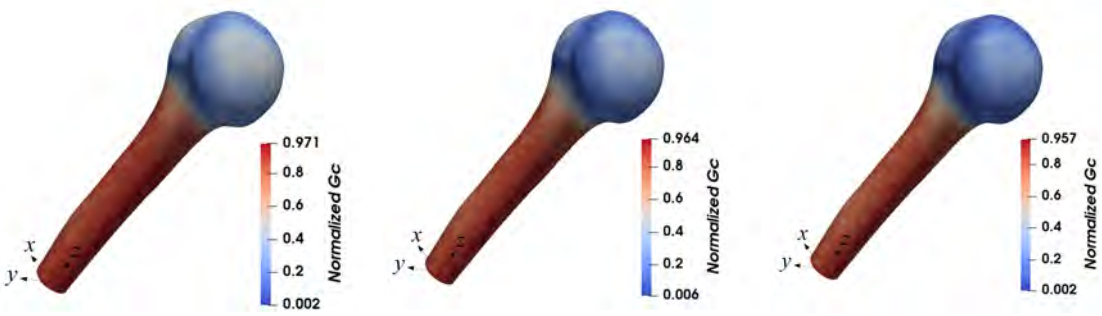

(a) $\beta = 0.8$ (b) $\beta = 1.0$ (c) $\beta = 1.2$

Figure 9: Variation of the normalized critical energy release rate according to the model in Eq. 4.4. Critical energy release rate is normalized by G_c^0.

4.4. Model calibration

The finite element and phase field methods have been implemented in FEAP 8.5 [81] with the linear solvers linked to the PETSc package [82]. The 3D mesh and inhomogeneous material properties is generated by Abaqus preprocessing tools [79] based on the QCT imaging techniques discussed in [7, 13]. The meshes along with the corresponding material properties are transferred to FEAP (as aforementioned using a python script), and post-processing is executed by calling the Paraview package [83]. Note that all simulations have been carried out in the High Performance Computing (HPC) cluster at Columbia University. At most four computing nodes were available for our simulations, that is , that is 96 cpus/processors, and the simulations had to be terminated after 6 hours of run time. In the following sections, we denote the physical modeling time (real time) by t and the actual simulation time (computer wall time) by CPU, which is used for parallel scalability studies. All simulations are performed under quasi-static conditions.

Following the model proposed in Yeni et al. [76] and other authors [68, 70], in all our simulations we assume a base critical energy release rate value of $G_c^0 = 7000$ J·m^{-2} defined in Eq. 4.4, and a maximum Young's modulus of $E_0 = 20$GPa.

4.4.1. Sensitivity of mesh size

We start by considering the fracture response of the model with different mesh densities. Previous studies (excluding fracture) [6, 15, 16, 84] suggested an element size of 3mm to accurately capture the heterogeneous variations in the mechanical properties of the bone. Hence, we analyze the response of the model considering an element size h of 1.2mm, 2mm and 3mm. The length scale size l_0 should be at least twice the mesh size

h [65, 85], therefore, we consider a constant length scale of $l_0 = 6$mm for all simulations. In addition the power-law parameter $\beta = 0.8$ is also assumed for the critical energy release rate value. If not mentioned otherwise, traction type loadings are applied on the bone head.

The strain-force curves are compared with the recorded strain-gauges output #8 (Fig. 10a) and # 12 (10b). Note that all strain measures are negative since they are obtained under compression, however, for convenience all strain plots in the paper are plotted in absolute value. The force F_z is the reaction force over the loading area along z direction. The results show that all meshes give consistent results for both strain gauges' locations. The slight differences may be due to a too coarse mesh that cannot describe accurately the heterogeneity. Nonetheless, the three different meshes give nearly same strength and approximately similar crack profiles as shown in Fig.10 and Fig. 11. In the following sections we choose the fine mesh to calibrate parameters and analyze the fracture response of the bone.

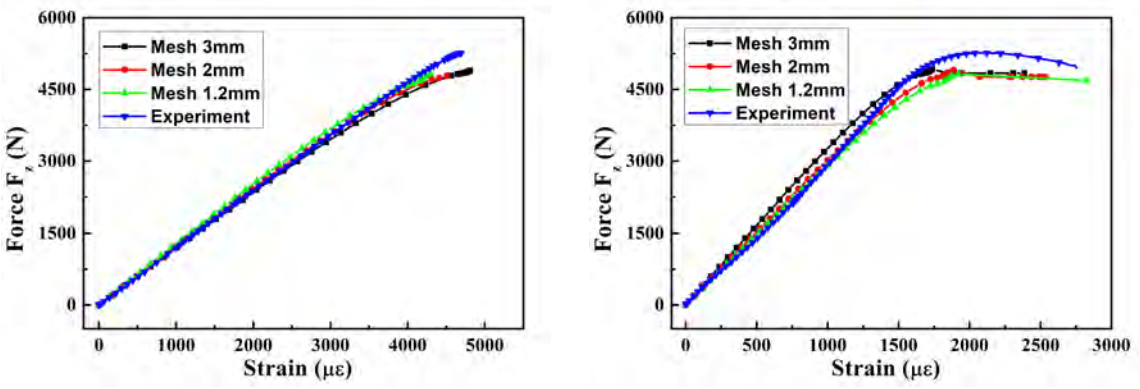

(a) SG #8 (b) SG #12

Figure 10: Strain-force relations for different mesh sizes at the two strain gauges locations. These curves are obtained under compression according to the experimental setup described in Section 4.1. For convenience, an absolute value of strain is used in all plots.

4.4.2. Sensitivity of the critical energy release rate

Many empirical relations for the critical energy G_c as function of the bone density ρ have been proposed, with a wide deviation between models [12, 68, 76, 84]. In this work, we propose a power-law dependence for critical energy release rate G_C as function of Young's modulus E (discussed in section 4) and calibrate the power-law parameter β.

Three different βs are investigated: 0.8 weak correlation ,1.0 linear correlation and 1.2 strong correlation. The length scale in this analysis is chosen as $l_0 = 3$mm.

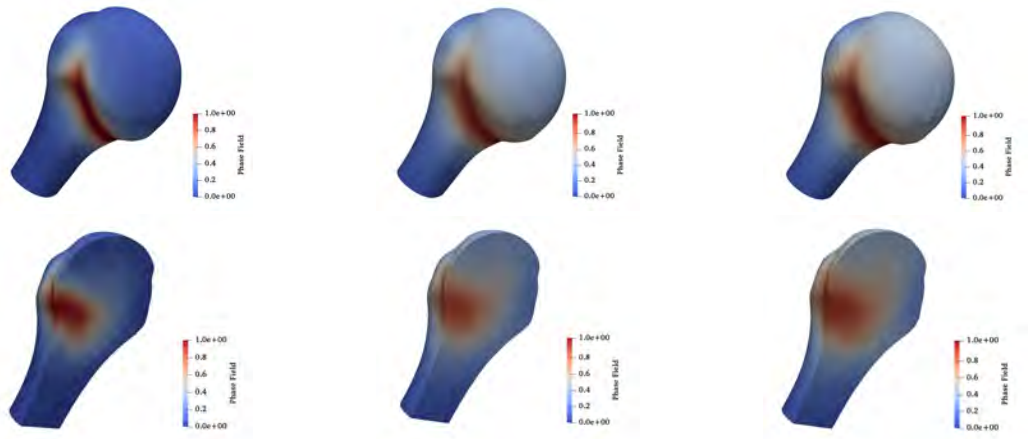

(a) $h = 1.2$mm, $u_z = 0.59$mm (b) $h = 2.0$mm, $u_z = 0.69$mm (c) $h = 3.0$mm, $u_z = 0.74$mm

Figure 11: Numerical crack profiles and the corresponding cross-sectional views for different mesh sizes h 1.2mm, 2mm and 3mm. u_z denotes the displacement along z direction of blue point A shown in Figure. 6(b).

It can be seen from Fig.12a, that the response of the bone up to failure for different β values match well with the experimental data, recorded by strain gauge #8. Hence the behavior is not sensitive to the value of β. However, indeed the β parameter dominates the failure response of the bone, as shown in Fig.12b and recorded by the strain gauge #12.

Hence, β has a significant effect on the strength of the material, which decreases with the increase of β. In other words, with $\beta > 1$ the inhomogeneous behaviour given by the ratio $\left(\frac{E}{E_0}\right)^{\beta} < 1$, is amplified, while $\beta < 1$ means that a lower level of inhomogeneous behavior in prescribed.

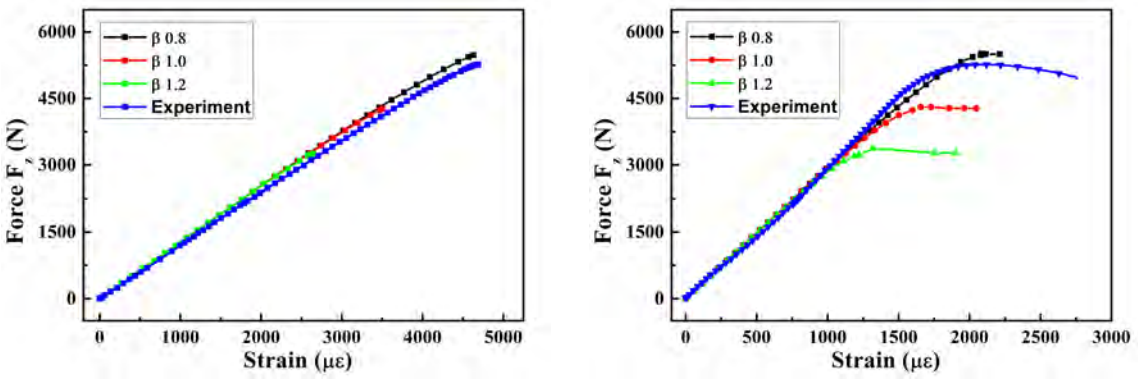

(a) SG #8 (b) SG #12

Figure 12: Strain force curves with different β at two strain-gauges.

Fig.13 shows cross sectional views of three different distribution of normalized G_c and

the corresponding crack patterns obtained with the simulations. Each of the simulations were stopped after 6 hours of run time which corresponds to different solution time t as denoted in the caption of the Figures. It can be seen that for the β values chosen, the final crack profiles are different although all cracks initiate at a similar location. It is interesting to note that while the parameter β doesn't affect the direction of crack propagation, it has a detrimental acceleration effect on the rate of crack propagation. That is, the larger the inhomogeneity of the critical energy release rate, the faster the crack propagation is. It should also be noted that for a constant G_c the crack profile obtained from the numerical model do not match the experimental results (see Appendix C for more details). Hence we conclude that for inhomogeneous materials the critical energy G_c must also be inhomogeneous, which was also discussed in Remark 3.

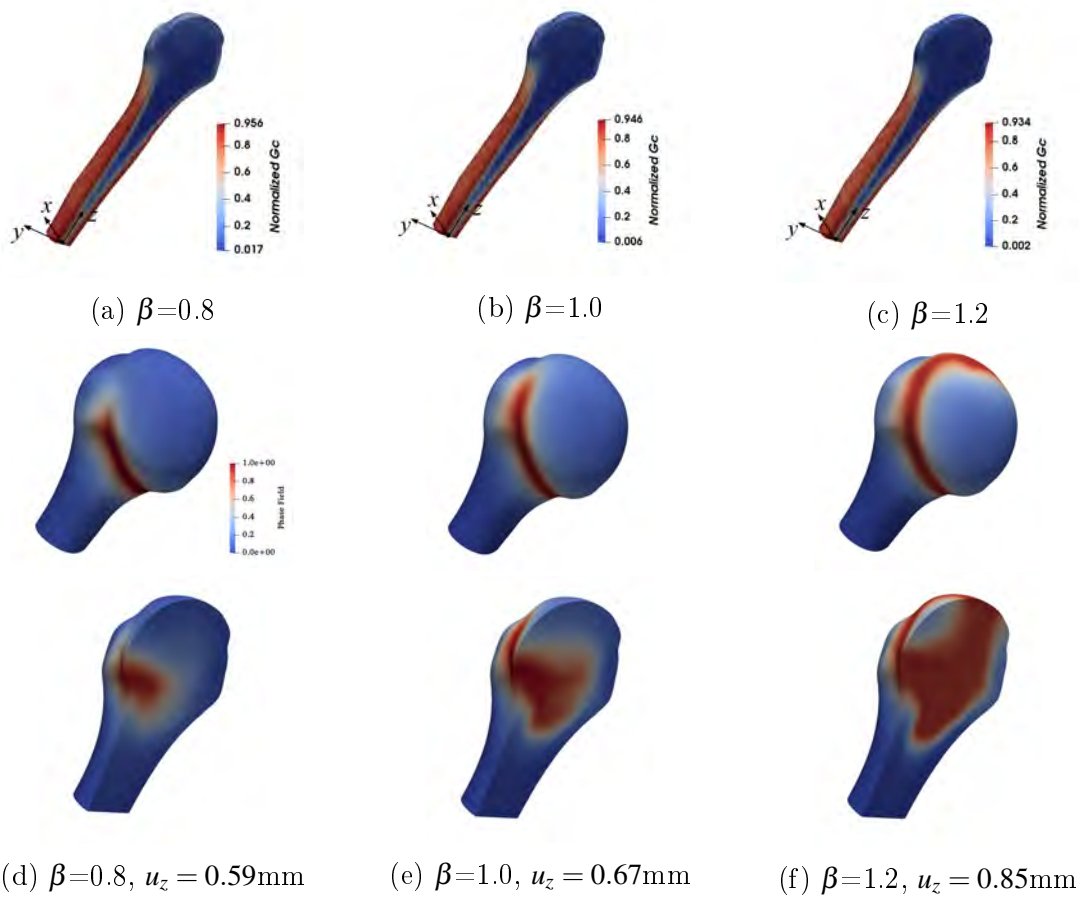

(a) β=0.8 (b) β=1.0 (c) β=1.2

(d) β=0.8, $u_z = 0.59$mm (e) β=1.0, $u_z = 0.67$mm (f) β=1.2, $u_z = 0.85$mm

Figure 13: Numerical examples for different β. (a)-(c) normalized critical energy release rate. Green dashed line denotes the boundary between cortical/trabecular bone; (d)-(f) Numerical crack profiles and cross sectional views of final cracks for different G_c. The same scale is used for all the plots.

Fig.14 shows the surface energy growth with respect to applied displacement recored on point A in Figure 6 (b) . These curves include two stages, initially damage is slowly

accumulated and suddenly all the strain energy is released followed by a rapid fracture propagation, which is a typical response of brittle fracture. Once again it can be seen that larger values of β lead to accelerated fracture initiation.

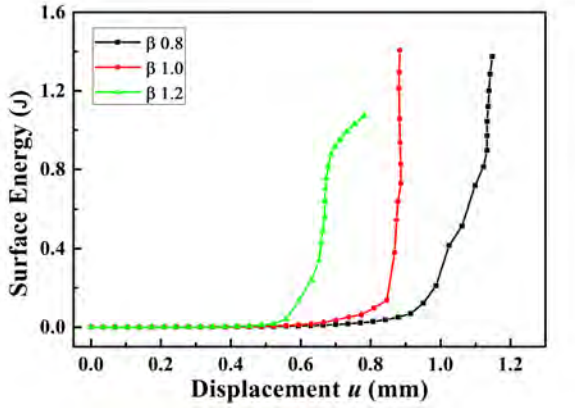

Figure 14: The effect of critical energy release rate variation on surface energy growth.

395 4.4.3. Length scale effects

In this section we study the effect of length scale l_0 on the simulation results. Different length scales could significantly affect the strength and the response of the material. In this part, three length scales 3mm, 6mm and 9mm are chosen and their affect on the strength of the bone is examined.

400 For all the simulations in this section, a fine mesh is used with an approximate element size of 1.2mm. The strain-force response of the material is shown and compared with the experimental data at strain gauges #8 and #12 and shown in Fig. 15a and 15b, respectively. One can observe that a larger length scale leads to lower strength. Such behaviour is also corroborated by one-dimensional simulations in case of homogeneous
405 materials [64].

The corresponding crack patterns for the different length scale l_0 are shown in Fig.16. As expected, the larger the length scale the more smeared the response is. Furthermore, a transition of the location of the cracked area can also be observed clearly. When the length scale is too large the point of crack initiation is shifted from the bone neck area
410 to the load area. While $l_0 = 3$mm generates the desired localized crack in the bone neck area, $l_0 = 6$mm leads to fracture of both the bone neck and load area causing the entire bone head to become damaged. The largest length scale $l_0 = 9$mm leads to damage in the region where the load is applied which means it cannot capture the correct crack behavior observed in the experiments. Hence, the length scale should be taken as small
415 as possible provided that at least two elements across the width should be used.

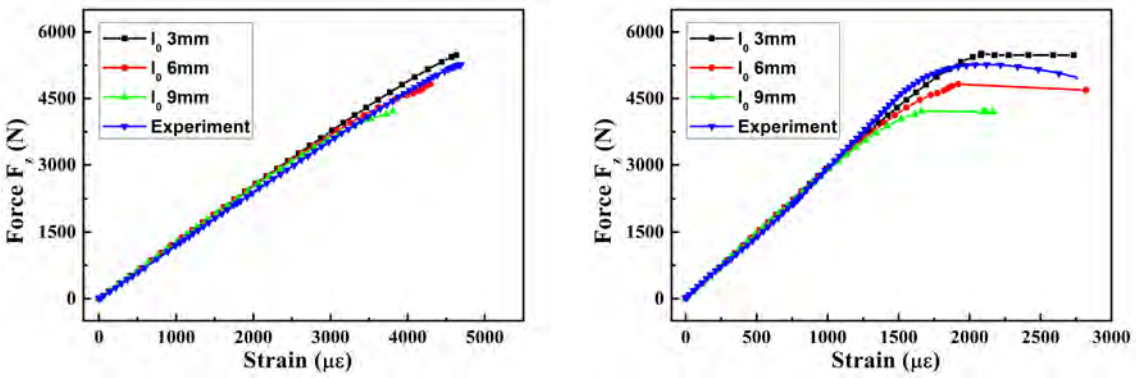

(a) SG #8 (b) SG #12

Figure 15: Strain-force curves with varying length scale l_0. (a) strain gauge #8, and (b) strain gauge #12.

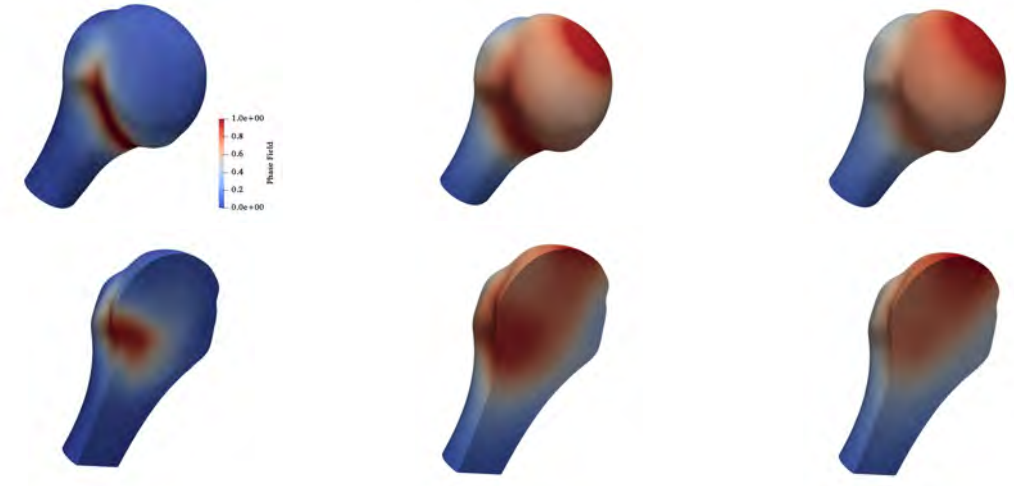

(a) l_0=3mm, $u_z = 0.59$mm (b) l_0=6mm, $u_z = 1.18$mm (c) l_0=9mm, $u_z = 1.00$mm

Figure 16: Numerical crack profiles and their cross sectional views for different length scale l_0. The same scale is used for all the plots.

4.4.4. Fracture profile

Now that the mesh size, length scale and critical energy release rate have been calibrated, a set of optimal parameters is selected as follows $h = 1.2$mm, $\beta = 0.8$, $l_0 = 3$mm. Fig.17 shows the predicted fracture evolution path with the aforementioned parameters as compared with the experimental testing, at three different stages of the bone deformation and fracture: initial, intermediate and final. The numerical results are plotted on the deformed configurations, magnified by a factor of 4. It can be observed that the numerical crack path agrees well with the experiments, where a shear-dominant failure behavior is observed.

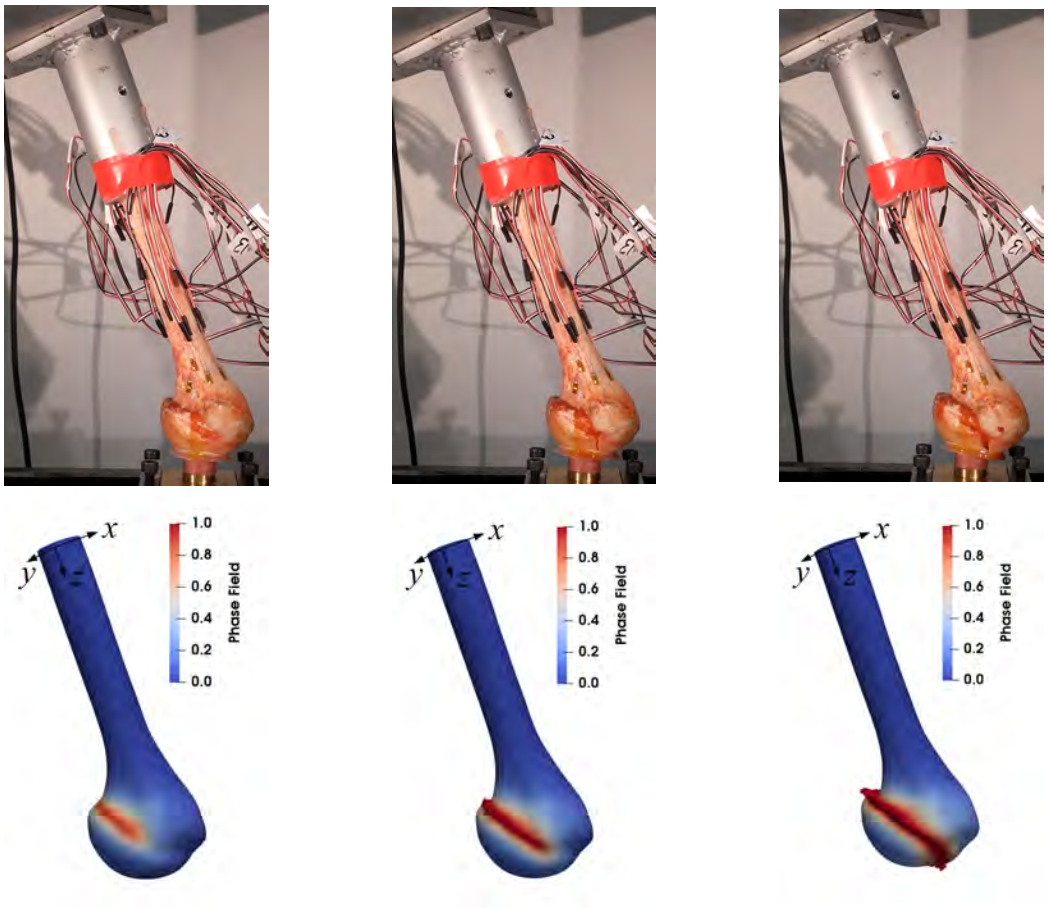

(a) $u_z = 0.46$mm (b) $u_z = 0.58$mm (c) $u_z = 0.86$mm

Figure 17: Comparison between experimental and numerical crack profiles at different stages of bone deformation and fracture. The numerical results are plotted on the deformed configuration, magnified by a factor of 4.

4.5. Further Studies

In this section, we present additional interesting fracture mechanics insights corresponding to the proposed phase field modeling approach. In particular we investigate the initiation and propagation of fracture and discuss the variation of principal stresses with the phase field evolution. We employ the calibrated parameters from previous sections, that is $\beta = 0.8, G_c^0 = 7000\text{J/m}^2$, $E_0 = 20\text{GPa}, l_0 = 3\text{mm}$ with a mesh size of $h = 1.2\text{mm}$. Poisson ratio of $\nu = 0.3$ is used for all the simulations.

4.5.1. Crack initiation and propagation

An interesting observation regarding crack initiation is illustrated in Fig. 18. It can be observed that the fracture is initiated at the trabecular part of the humerus head (inside the bone) and then propagates outwards toward the cortical outer surface bone until it completely fractures. Although this behavior cannot be confirmed experimentally, it is still reasonable to assume that the load is being transferred to the trabecular structure inside the head, causing the trabeculae to fracture first and only then propagates to the cortical surface, the very thin cortical layer covering the bone's head [86].

We emphasize that it is the first time that such behaviour is numerically confirmed.

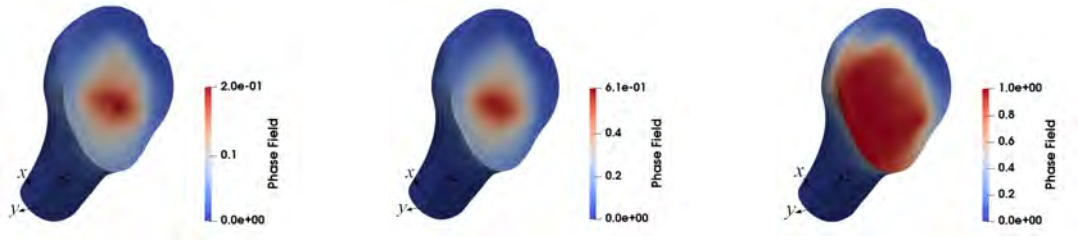

(a) $u_z = 0.26\text{mm}$ (b) $u_z = 0.34\text{mm}$ (c) $u_z = 0.59\text{mm}$

Figure 18: Snapshots of the evolution of the fracture process in the 67 years old humerus bone.

4.5.2. Principal directions

In the experiments conducted in [73], the strain-gauges were placed along the expected principal directions. Hence, since a linear elastic analysis is carried out, the principal directions remain unchanged. However, in this section we show that when damage/fracture is involved, the principal directions of the model rotate as function the accumulated damage at the particular point.

To this end, Fig.19 shows the variation of principal angles from the original directions as function of the phase field value at strain gauges #8 and #12. The change in angles

θ_{jj} between the original/damaged principal directions is defined as

$$cos(\theta_{jj}) = \frac{\boldsymbol{n}_j \cdot \boldsymbol{n}_j^i}{\|\boldsymbol{n}_j\| \|\boldsymbol{n}_j^i\|} \tag{4.5}$$

where $j = 1,2,3$ denote the three directions. $\boldsymbol{n}_j^i$ are the initial principal coordinates vectors and $\boldsymbol{n}_j$ the current principal coordinates vectors.

It can be seen that the change in angles remain nearly zero when the phase field is relatively small. However, as damage grows, the principal directions may significantly change at both strain gauge locations.

Remark 4: In the current paper, we use principal strain ε_3 as the strain measure to compare with the experimental results. It can be observed that the change of third principal direction is less than 15 degrees, which means current measure is still reasonable. The strong oscillations shown in the figure may due to the inhomogeneity of bone.

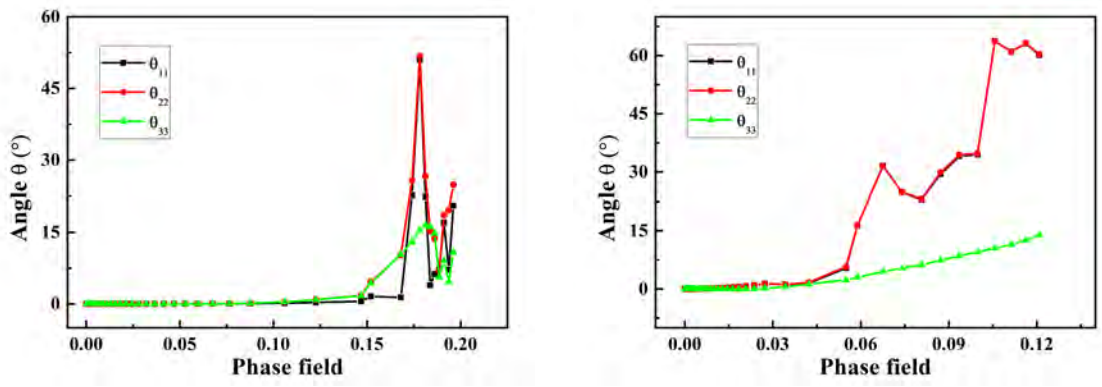

(a) SG #8 (b) SG #12

Figure 19: Principal angles change with the increase of damage/phase field variable.

4.6. Parallel Scalability

Finally, we demonstrate the parallel scalability of the proposed phase field implementation, which is necessary due to the very fine meshes required for bone modeling. The fine mesh tetrahedral bone model, which contains 323,543 elements, 58,885 nodes and 235,540 degrees of freedom is solved on five different sets of processors: 12, 24, 48, 72 and 96. For illustration, the partition of the bone to 48 processors and the corresponding slice are shown in Fig.20(a)-(b).

As aforementioned, the simulations in previous sections have been terminated after 6 hours run on the HPC at Columbia University. However, in this section we run all simulations up to 20 seconds of physical time, which needs less than 6 hours to complete. A direct LU solver is employed to solve the nonlinear Jacobian system using the PETSc package [82]. Table 1 shows the CPU time cost corresponding to the number of processors. It can be seen that the CPU time increases with decreasing number of processors.

Table 1: Comparison of CPU time[s] (simulation wall time) for different processors with fixed problem size (235,540 degrees of freedom), terminated after t=20s physical time.

Processors	1	12	24	48	72	96
CPU time(s)	15778.18	1810.36	922.71	566.66	409.09	402.43

Fig. 20(c) and (d) are used to show the speedup and scalability of our parallel implementation. The CPU time of single processor is used as the reference time in current studies. The dash line denotes the ideal linear speedup. It can be seen that as the number of processors increases, the speedup that can be achieved stagnates and the efficiency decreases. This has to do with the processors communications, system hardware and algorithm scalability and requires further computer science research into more efficient solvers, which will be part of future work.

5. Conclusions

A novel modification of the phase field fracture method with application to fracture of the humerus bone within a finite element framework, was proposed. CT-scans were employed to generate detailed finite element bone meshes with corresponding inhomogeneous material properties. The implementation of the method was verified using the method of manufactured solutions(MMS) and validated by experiments.

To model the fracture, we proposed a power law relationship between bone density and the critical energy release rate, together with a volumetric-deviatoric type split of the elastic energy that drives the fracture evolution. Several parameters of the method, including mesh size, length scale and inhomogeneous critical energy release rate were calibrated based on humeri experiments on a 67 year old male bone. With these calibrated parameters it was shown that the proposed numerical method is able to successfully predict the fracture initiation and propagation, which agree well with the experimental observations.

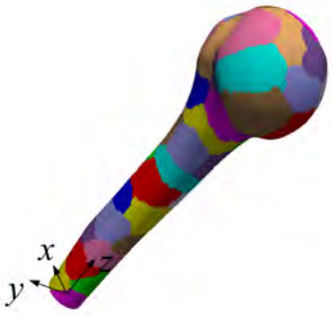

(a) Partitions of the mesh to 48 processors.

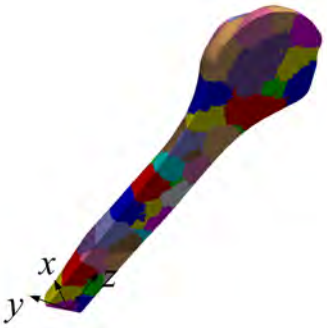

(b) Slice of the bone with 48 partitions.

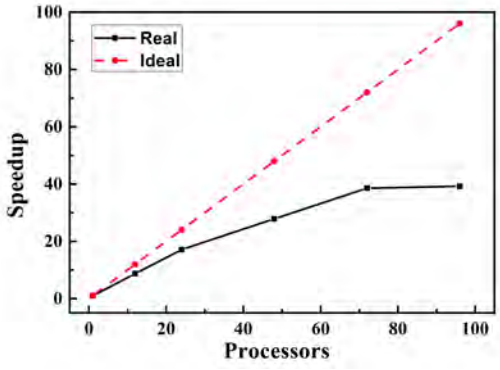

(c) Speedup

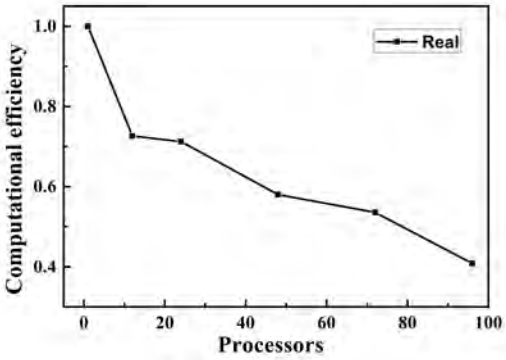

(d) Computational efficiency

Figure 20: Parallel Scalability of the phase field implementation for bone fracture studies.

An interesting finding confirms that fracture initiation occurs at the inner trabecular bone and propagates outwards toward the cortical bone. Furthermore, we show that when fracture analysis is carried out, the principal directions at a point rotate with the amount of accumulated damage, which is overlooked when linear elastic analysis with stress criteria is used to study bone fracture.

Nonetheless, some limitations of the modeling need further studies. For example, the results are somewhat sensitive to the length scale l_0. In future work we will consider a variation of the length scale with the bone Young's modulus values. The method was implemented in a parallel high performance computing environment at Columbia University and scalability studies were carried out. However, the scalability results indicate that further research on efficient parallel solvers is also required.

To the authors knowledge, this work is the first successful attempt to apply the phase field fracture method to study bone fracture. In the future such numerical tool may become an invaluable tool for patient-specific medicine. For example, the effect of an implant inserted into the bone could be quantitatively assessed before an actual procedure is recommended by the surgeon.

Acknowledgment

We acknowledge computing resources from Columbia University's Shared Research Computing Facility project, which is supported by NIH Research Facility Improvement Grant 1G20RR030893-01, and associated funds from the New York State Empire State Development, Division of Science Technology and Innovation (NYSTAR) Contract C090171. The first author would like to acknowledge the financial support from China Scholarship Council (CSC) (201606120064) for his two-year visit to Columbia University where this collaborative work was carried out.

Appendix A. Strain gauges' positions

We present the strain gauges position in the experiments. All the coordinates are obtained in the numerical global coordinates system. Because the gauges are rectangular shape, the coordinates of two corner points are needed to determine its location that are shown in Table.A.2. The direction of the obtain strain can then be obtained approximately.

Table A.2: Strain gauges' position (unit: mm)

Strain gauges	x	y	z
#8	-15.02	0.75	107.67
	-16.14	0.63	110.87
#12	7.49	9.97	118.29
	7.45	11.49	121.53

Appendix B. Transformation matrix

In order to define the surface traction, a local coordinate system is introduced. The transformation matrix can be expressed

$$T = \begin{bmatrix} T_{11} & T_{12} & T_{13} \\ T_{21} & T_{22} & T_{23} \\ T_{31} & T_{32} & T_{33} \end{bmatrix} = \begin{bmatrix} 0.8646 & -0.3794 & 0.3293 \\ -0.3939 & -0.9188 & -0.0245 \\ 0.3119 & -0.1085 & -0.9439 \end{bmatrix} \tag{B.1}$$

Additional translation is also needed, that is (-22.63, 7.41, 162.3)mm, which is the global coordinates of the origin of local load system.

Appendix C. Fracture profile with constant critical energy release rate

In this section, we illustrate the behavior of the standard phase field method [35–46], which assumes a constant critical fracture energy G_c, on the bone fracture considered in this paper. Hence, we choose $\beta = 0.0$ in the power law relation defined in Eq.4.4,and all other material parameters are chosen to be the same as the one in section 4.4.4. Fig.C.21 shows the final phase field accumulation and crack path in the bone. It can clearly be seen that a constant G_c leads to fracture of the bone-neck, which is quite different from the experimental results presented in section 4.4.4. Hence, the proposed power-law model for critical energy release rate G_c is necessary and able to capture the complex bone fracture profile.

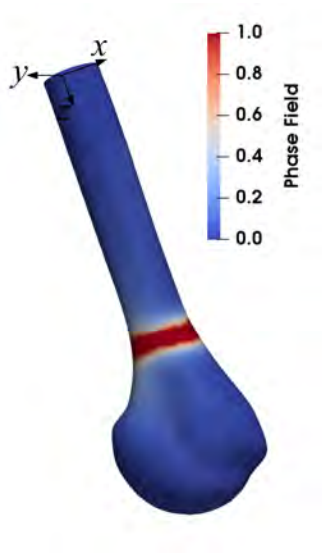

Figure C.21: Bone-fracture profile with a standard phase field method (constant G_c)

References

[1] R. Nalla, J. Stölken, J. Kinney, R. Ritchie, Fracture in human cortical bone: local fracture criteria and toughening mechanisms, Journal of biomechanics 38 (7) (2005) 1517–1525.

[2] X. Wang, S. Puram, The toughness of cortical bone and its relationship with age, Annals of Biomedical Engineering 32 (1) (2004) 123–135.

[3] J. H. Keyak, M. G. Fourkas, J. M. Meagher, H. B. Skinner, Validation of an automated method of three-dimensional finite element modelling of bone, Journal of Biomedical Engineering 15 (6) (1993) 505–509.

[4] J. Op Den Buijs, D. Dragomir-Daescu, Validated finite element models of the proximal femur using two-dimensional projected geometry and bone density, Computer Methods and Programs in Biomedicine 104 (2) (2011) 168–174.

[5] H. S. Hosseini, A. L. Clouthier, P. K. Zysset, Experimental validation of finite element analysis of human vertebral collapse under large compressive strains, Journal of biomechanical engineering 136 (4) (2014) 041006.

[6] R. Hambli, S. Allaoui, A robust 3D finite element simulation of human proximal femur progressive fracture under stance load with experimental validation, Annals of Biomedical Engineering 41 (12) (2013) 2515–2527.

[7] Z. Yosibash, N. Trabelsi, C. Milgrom, Reliable simulations of the human proximal femur by high-order finite element analysis validated by experimental observations, Journal of biomechanics 40 (16) (2007) 3688–3699.

[8] Z. Yosibash, R. P. Mayo, G. Dahan, N. Trabelsi, G. Amir, C. Milgrom, Predicting the stiffness and strength of human femurs with real metastatic tumors, Bone 69 (2014) 180–190.

[9] N. K. Knowles, J. M. Reeves, L. M. Ferreira, Quantitative computed tomography (QCT) derived bone mineral density (bmd) in finite element studies: a review of the literature, J Exp Orthop 3 (1) (2016) 36.

[10] E. Dall'Ara, B. Luisier, R. Schmidt, F. Kainberger, P. Zysset, D. Pahr, A nonlinear QCT-based finite element model validation study for the human femur tested in two configurations in vitro, Bone 52 (1) (2013) 27–38.

[11] T. Rossman, V. Kushvaha, D. Dragomir-Daescu, QCT/FEA predictions of femoral stiffness are strongly affected by boundary condition modeling, Computer methods in biomechanics and biomedical engineering 19 (2) (2016) 208–216.

[12] D. Dragomir-Daescu, J. Op Den Buijs, S. McEligot, Y. Dai, R. C. Entwistle, C. Salas, L. J. Melton, K. E. Bennet, S. Khosla, S. Amin, Robust QCT/FEA models of proximal femur stiffness and fracture load during a sideways fall on the hip, Annals of Biomedical Engineering 39 (2) (2011) 742–755.

[13] Z. Yosibash, R. Padan, L. Joskowicz, C. Milgrom, A CT-based high-order finite element analysis of the human proximal femur compared to in-vitro experiments, Journal of biomechanical engineering 129 (3) (2007) 297–309.

[14] D. H. Pahr, P. K. Zysset, From high-resolution CT data to finite element models: development of an integrated modular framework, Computer methods in biomechanics and biomedical engineering 12 (1) (2009) 45–57.

[15] J. E. M. Koivumäki, J. Thevenot, P. Pulkkinen, V. Kuhn, T. M. Link, F. Eckstein, T. Jämsä, Ct-based finite element models can be used to estimate experimentally measured failure loads in the proximal femur, Bone 50 (4) (2012) 824–829.

[16] M. Bessho, I. Ohnishi, J. Matsuyama, T. Matsumoto, K. Imai, K. Nakamura, Prediction of strength and strain of the proximal femur by a ct-based finite element method, Journal of Biomechanics 40 (8) (2007) 1745–1753.

[17] Z. Yosibash, K. Myers, Y. Levi, Computational bone mechanics: From the cloud to an orthopedists mobile device 105 (2015) 235–249.

[18] R. O. Ritchie, M. J. Buehler, P. Hansma, Plasticity and toughness in bone.

[19] A. Ural, D. Vashishth, Cohesive finite element modeling of age-related toughness loss in human cortical bone, Journal of biomechanics 39 (16) (2006) 2974–2982.

[20] A. Licata, Bone density vs bone quality: What's a clinician to do?, Cleveland Clinic journal of medicine 76 (6) (2009) 331–336.

[21] G. Dahan, N. Trabelsi, O. Safran, Z. Yosibash, Verified and validated finite element analyses of humeri, Journal of Biomechanics 49 (7) (2016) 1094–1102.

[22] D. Taylor, T. C. Lee, A crack growth model for the simulation of fatigue in bone, International Journal of Fatigue 25 (5) (2003) 387–395.

[23] J. H. Keyak, S. A. Rossi, Prediction of femoral fracture load using finite element models: an examination of stress- and strain-based failure theories, Journal of Biomechanics 33 (2) (2000) 209–214.

[24] R. Hambli, A quasi-brittle continuum damage finite element model of the human proximal femur based on element deletion, Medical biological engineering computing 51 (1-2) (2013) 219–231.

[25] R. Hambli, A. Bettamer, S. Allaoui, Finite element prediction of proximal femur fracture pattern based on orthotropic behaviour law coupled to quasi-brittle damage, Medical Engineering & Physics 34 (2) (2012) 202–210.

[26] R. Hambli, Micro-CT finite element model and experimental validation of trabecular bone damage and fracture, Bone 56 (2) (2013) 363–374.

[27] N. M. Harrison, P. McDonnell, L. Mullins, N. Wilson, D. O'Mahoney, P. E. McHugh, Failure modelling of trabecular bone using a non-linear combined damage and fracture voxel finite element approach, Biomechanics and Modeling in Mechanobiology 12 (2) (2013) 225–241.

[28] A. Ural, S. Mischinski, Multiscale modeling of bone fracture using cohesive finite elements, Engineering Fracture Mechanics 103 (2013) 141–152.

[29] A. A. Abdel-Wahab, V. V. Silberschmidt, Numerical modelling of impact fracture of cortical bone tissue using x-fem, Journal of Theoretical and Applied Mechanics 49 (2011) 599–619.

[30] J. Fish, N. Hu, Multiscale modeling of femur fracture, International Journal for Numerical Methods in Engineering 111 (1) (2017) 3–25.

[31] S. Li, A. Abdel-Wahab, V. V. Silberschmidt, Analysis of fracture processes in cortical bone tissue, Engineering Fracture Mechanics 110 (Supplement C) (2013) 448–458.

[32] P. Grassl, M. Jirásek, On mesh bias of local damage models for concrete, Proceedings of FraMCoS-5, Vail, USA (2004) 252–262.

[33] J.-J. Marigo, C. Maurini, K. Pham, An overview of the modelling of fracture by gradient damage models, Meccanica 51 (12) (2016) 3107–3128.

[34] J. Londono, L. Berger-Vergiat, H. Waisman, An equivalent stress-gradient regularization model for coupled damage-viscoelasticity, Computer Methods in Applied Mechanics and Engineering 322 (Supplement C) (2017) 137–166.

[35] H. Amor, J.-J. Marigo, C. Maurini, Regularized formulation of the variational brittle fracture with unilateral contact: Numerical experiments, Journal of the Mechanics and Physics of Solids 57 (8) (2009) 1209–1229.

[36] M. J. Borden, C. V. Verhoosel, M. A. Scott, T. J. R. Hughes, C. M. Landis, A phase-field description of dynamic brittle fracture, Computer Methods in Applied Mechanics and Engineering 217-220 (2012) 77–95.

[37] B. Bourdin, G. A. Francfort, J. J. Marigo, Numerical experiments in revisited brittle fracture, Journal of the Mechanics and Physics of Solids 48 (4) (2000) 797–826.

[38] F. P. Duda, A. Ciarbonetti, P. J. Sánchez, A. E. Huespe, A phase-field/gradient damage model for brittle fracture in elastic-plastic solids, International Journal of Plasticity 65 (2015) 269–296.

[39] J. Vignollet, S. May, R. de Borst, C. V. Verhoosel, Phase-field models for brittle and cohesive fracture, Meccanica 49 (11) (2014) 2587–2601.

[40] C. Kuhn, R. Müller, Crack nucleation in phase field fracture models, in: ICF13, 2013.

[41] S. May, J. Vignollet, R. de Borst, A numerical assessment of phase-field models for brittle and cohesive fracture: OY-convergence and stress oscillations, European Journal of Mechanics - A/Solids 52 (2015) 72–84.

[42] C. Miehe, F. Welschinger, M. Hofacker, Thermodynamically consistent phase-field models of fracture: Variational principles and multi-field fe implementations, International Journal for Numerical Methods in Engineering 83 (10) (2010) 1273–1311.

[43] A. Karma, D. A. Kessler, H. Levine, Phase-field model of mode III dynamic fracture, Physical Review Letters 87 (4) (2001) 045501.

[44] A. Karma, A. E. Lobkovsky, Unsteady crack motion and branching in a phase-field model of brittle fracture, Physical review letters 92 (24) (2004) 245510.

[45] L. Eastgate, J. P. Sethna, M. Rauscher, T. Cretegny, C.-S. Chen, C. Myers, Fracture in mode i using a conserved phase-field model, Physical Review E 65 (3) (2002) 036117.

[46] C. McAuliffe, H. Waisman, A unified model for metal failure capturing shear banding and fracture, International Journal of Plasticity 65 (2015) 131–151.

[47] A. A. Griffith, The phenomena of rupture and flow in solids, Philosophical Transactions of the Royal Society London, Series A 221 (1921) 163–198.

[48] L.-M. Schanzel, Phase field modeling of fracture in rubbery and glassy polymers at finite thermo-viscoelastic deformations, Thesis (2015).

[49] R. Shen, H. Waisman, L. Guo, Fracture of viscoelastic solids modeled with a modified phase field method, Computer Methods in Applied Mechanics and Engineering 346 (2019) 862–890.

[50] T. T. Nguyen, J. Yvonnet, M. Bornert, C. Chateau, Initiation and propagation of complex 3d networks of cracks in heterogeneous quasi-brittle materials: Direct comparison between in situ testing-microct experiments and phase field simulations, Journal of the Mechanics and Physics of Solids 95 (2016) 320–350.

[51] T.-T. Nguyen, J. RΓκthorΓκ, J. Yvonnet, M.-C. Baietto, Multi-phase-field modeling of anisotropic crack propagation for polycrystalline materials, Computational Mechanics 60 (2) (2017) 289–314.

[52] C. Miehe, M. Hofacker, F. Welschinger, A phase field model for rate-independent crack propagation: Robust algorithmic implementation based on operator splits, Computer Methods in Applied Mechanics and Engineering 199 (45-48) (2010) 2765–2778.

[53] M. Arriaga, H. Waisman, Combined stability analysis of phase-field dynamic fracture and shear band localization, International Journal of Plasticity 96 (2017) 81–119.

[54] Z. A. Wilson, C. M. Landis, Phase-field modeling of hydraulic fracture, Journal of the Mechanics and Physics of Solids 96 (2016) 264–290.

[55] Y. Heider, B. Markert, A phase-field modeling approach of hydraulic fracture in saturated porous media, Mechanics Research Communications 80 (2017) 38–46.

[56] C. Miehe, S. Mauthe, Phase field modeling of fracture in multi-physics problems. part iii. crack driving forces in hydro-poro-elasticity and hydraulic fracturing of fluid-saturated porous media, Computer Methods in Applied Mechanics and Engineering 304 (2016) 619–655.

[57] M. Paggi, J. Reinoso, Revisiting the problem of a crack impinging on an interface:a modeling framework for the interaction between the phase field approach for brittle fracture and the interface cohesive zone model, Computer Methods in Applied Mechanics and Engineering 321 (2017) 145–172.

[58] T. T. Nguyen, J. Yvonnet, Q. Z. Zhu, M. Bornert, C. Chateau, A phase-field method for computational modeling of interfacial damage interacting with crack propagation in realistic microstructures obtained by microtomography, Computer Methods in Applied Mechanics and Engineering 312 (2016) 567–595.

[59] S. Teichtmeister, D. Kienle, F. Aldakheel, M.-A. Keip, Phase field modeling of fracture in anisotropic brittle solids, International Journal of Non-Linear Mechanics 97 (2017) 1–21.

[60] T. T. Nguyen, J. Réthoré, M.-C. Baietto, Phase field modelling of anisotropic crack propagation, European Journal of Mechanics - A/Solids 65 (2017) 279–288.

[61] R. de Borst, C. V. Verhoosel, Gradient damage vs phase-field approaches for fracture: Similarities and differences, Computer Methods in Applied Mechanics and Engineering 312 (2016) 78–94.

[62] M. J. Borden, Isogeometric analysis of phase-field models for dynamic brittle and ductile fracture, Thesis (2012).

[63] M. A. Msekh, J. M. Sargado, M. Jamshidian, P. M. Areias, T. Rabczuk, Abaqus implementation of phase-field model for brittle fracture, Computational Materials Science 96, Part B (2015) 472–484.

[64] X. Zhang, C. Vignes, S. W. Sloan, D. Sheng, Numerical evaluation of the phase-field model for brittle fracture with emphasis on the length scale, Computational Mechanics (2017) 1–16.

[65] X. Zhang, S. W. Sloan, C. Vignes, D. Sheng, A modification of the phase-field model for mixed mode crack propagation in rock-like materials, Computer Methods in Applied Mechanics and Engineering 322 (2017) 123–136.

[66] M. Arriaga, H. Waisman, Stability analysis of the phase-field method for fracture with a general degradation function and plasticity induced crack generation, Mechanics of Materials 116 (2018) 33–48.

[67] K. J. Koester, J. A. Iii, R. Ritchie, The true toughness of human cortical bone measured with realistically short cracks, Nature materials 7 (8) (2008) 672.

[68] Y. N. Yeni, T. L. Norman, Fracture toughness of human femoral neck: effect of microstructure, composition, and age, Bone 26 (5) (2000) 499–504.

[69] T. L. Norman, D. Vashishth, D. B. Burr, Fracture toughness of human bone under tension, Journal of Biomechanics 28 (3) (1995) 309–320.

[70] J. Yan, A. Daga, R. Kumar, J. J. Mecholsky, Fracture toughness and work of fracture of hydrated, dehydrated, and ashed bovine bone, Journal of Biomechanics 41 (9) (2008) 1929–1936.

[71] K. Salari, P. Knupp, Code verification by the method of manufactured solutions, Report, Sandia National Labs., Albuquerque, NM (US); Sandia National Labs., Livermore, CA (US) (2000).

[72] P. J. Roache, Code verification by the method of manufactured solutions, Journal of Fluids Engineering 124 (1) (2001) 4–10.

[73] G. Dahan, N. Trabelsi, O. Safran, Z. Yosibash, Finite element analyses for predicting anatomical neck fractures in the proximal humerus, under review.

[74] G. Wu, F. C. T. van der Helm, H. E. J. Veeger, M. Makhsous, P. Van Roy, C. Anglin, J. Nagels, A. R. Karduna, K. McQuade, X. Wang, F. W. Werner, B. Buchholz, Isb recommendation on definitions of joint coordinate systems of various joints for the reporting of human joint motion-part ii: shoulder, elbow, wrist and hand, Journal of Biomechanics 38 (5) (2005) 981–992.

[75] J. C. Behiri, W. Bonfield, Fracture mechanics of bone - The effects of density, specimen thickness and crack velocity on longitudinal fracture, Journal of Biomechanics 17 (1) (1984) 25–34.

[76] Y. N. Yeni, C. U. Brown, T. L. Norman, Influence of bone composition and apparent density on fracture toughness of the human femur and tibia, Bone 22 (1) (1998) 79–84.

[77] T. S. Keller, Predicting the compressive mechanical behavior of bone, Journal of Biomechanics 27 (9) (1994) 1159–1168.

[78] M. E. Launey, M. J. Buehler, R. O. Ritchie, On the mechanistic origins of toughness in bone, Annual review of materials research 40 (2010) 25–53.

[79] Abaqus user documentation. v6.12 (2012).

[80] R. O. Ritchie, The conflicts between strength and toughness, Nature Materials 10 (11) (2011) 817–22.

[81] R. L. Taylor, FEAP - Finite Element Analysis Program (2017).

[82] S. Balay, W. D. Gropp, L. C. McInnes, B. F. Smith, Efficient Management of Parallelism in Object-Oriented Numerical Software Libraries, Birkhäuser Boston, Boston, MA, 1997, pp. 163–202.

[83] J. Ahrens, B. Geveci, C. Law, 36 - ParaView: An End-User Tool for Large-Data Visualization A2 - Hansen, Charles D, Butterworth-Heinemann, Burlington, 2005, pp. 717–731.

[84] J. H. Keyak, H. B. Skinner, Three-dimensional finite element modelling of bone: effects of element size, Journal of Biomedical Engineering 14 (6) (1992) 483–489.

[85] M. Klinsmann, D. Rosato, M. Kamlah, R. M. McMeeking, An assessment of the phase field formulation for crack growth, Computer Methods in Applied Mechanics and Engineering 294 (2015) 313–330.

[86] Z. Yosibash, R. P. Mayo, C. Milgrom, Atypical viscous fracture of human femurs, Adv Biomech Appl 1 (2) (2014) 77–83.